Applied Catalysis B: Environmental 129 (2013) 416–425

Contents lists available at SciVerse ScienceDirect

Applied Catalysis B: Environmental

journal homepage: www.elsevier.com/locate/apcatb

Microreactors based on CuO–CeO_2/zeolite films synthesized onto brass microgrids for the oxidation of CO

Nicolás C. Pérez, Eduardo E. Miró, Juan M. Zamaro*

Instituto de Investigaciones en Catálisis y Petroquímica, INCAPE (FIQ, UNL-CONICET) Santiago del Estero 2829, 3000 Santa Fe, Argentina

ARTICLE INFO

Article history:
Received 15 June 2012
Received in revised form
20 September 2012
Accepted 28 September 2012
Available online 8 October 2012

Keywords:
Microreactor
Brass support
Mordenite
Wire mesh
Total CO oxidation
Preferential CO oxidation

ABSTRACT

Microreactors based on Cu, Ce oxides dispersed onto zeolite films grown on brass microgrids were developed. Secondary synthesis conditions were regulated in order to obtain thin, homogeneous and adherent coatings of mordenite to which Cu and Ce were later incorporated. The systems were characterized by XRD, SEM-EPMA, H_2-TPR, LRS and XPS. The catalytic coatings were mechanically and chemically stable under reaction. Cu, Ce/zeolite microreactors were evaluated in the CO total oxidation (COTox) and in the preferential CO oxidation (COProx) showing a superior performance when compared with the same powder catalyst.

1. Introduction

The miniaturization of structured catalysts in the micro-scale range offers important advantages when used in industrial catalytic processes. This is due to the great increase in mass and heat transfer coefficients as compared with conventional reactors [1]. In gas phase reactions, this implies controlling highly exothermic or endothermic reactions which are difficult to manipulate in traditional reactors [2]. Moreover, because of their high surface/volume ratios, small reaction volumes are involved, generating short residence times which increase the efficiency and selectivity of processes [3]. Nowadays, with the help of available microfabrication techniques, microreactors can be made in various materials and with diverse design concepts. The use of metallic substrates could bring some advantages, such as the possibility of achieving thin catalytic walls, high mechanical resistance, and versatility to adopt different configurations in the shape and size of the microchannels. Although silicon and stainless steel are the materials most widely reported as supports in the literature [1–3], when exothermic reactions are involved it would be better to employ a material with higher thermal conductivity, as demonstrated by Groppi et al. for structured catalysts of millimetric scale [4]. For microreactors, molybdenum and aluminum alloys have been employed as supports [5–7], as well as thin brass wires packed into tubular millimeter-sized reactors [8] and brass micromonoliths employed for the ethyl acetate combustion [9]. Brass has high specific thermal conductivity, high thermal diffusivity and low specific heat [10]. Additionally, it is a non-expensive, readily available material.

On the other hand, zeolites are microporous materials that can be employed in a broad variety of reactions and they have high thermal stability and reproducibility of synthesis. Despite these advantages, the coating of microchannels with zeolites [11–16] or the catalytic application of zeolite-based microreactors have not been so widely reported in the literature [5,16–22]. A key factor to successfully design zeolite-based microreactors is the obtention of thin, uniform and adherent zeolite films in the microreactor channels which should be smaller than 500 μm. Subsequently, a variety of active metal species can be introduced in the microporous films, as exchanged metal atoms or dispersed oxide phases. The synthesis of zeolite films on flat substrates of Cu and Cu alloys has been reported in the pioneering works of Davis et al. [23], and Mintova et al. [24–26]. Davis et al. [23] synthesized zeolite Y coatings on Cu foils and analyzed the effect of various treatments on the adherence. Mintova et al. and Valtchev and co-workers [24–26] also studied the synthesis of zeolite films (Zeolite Y, ZSM-5, Silicalite-1 and SAPO-5) on substrates of copper and brass. Furthermore, zeolite 4A has been synthesized on copper foams with small pores [27]. More recently, we have shown the synthesis of uniform and

* Corresponding author. Tel.: +54 0342 4536861; fax: +54 0342 4536861.
E-mail address: zamaro@fiq.unl.edu.ar (J.M. Zamaro).

0926-3373/$ – see front matter © 2012 Elsevier B.V. All rights reserved.
http://dx.doi.org/10.1016/j.apcatb.2012.09.058

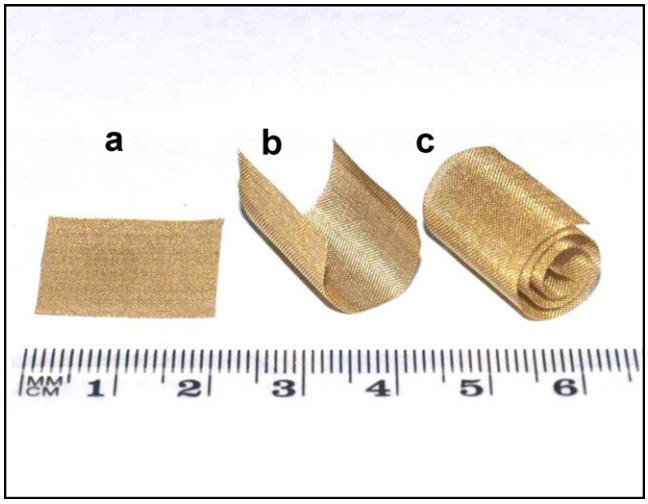

Fig. 1. Pictures of the seeded microgrids before the hydrothermal treatment: (a) planar-shaped, (b) U-shaped and (c) spiral-shaped.

thin mordenite films confined into microchannels formed in brass plates [16].

The CO oxidation is an exothermic reaction with environmental interest. On the one hand, it is an extremely toxic gas that accumulates indoors and must be eliminated (COTox) [28]. On the other hand, in the field of clean energy, CO must be removed from H_2 streams to be used in power cells (COProx) [29]. Although highly active catalysts based on Au and Pt have been studied for the later reaction [30,31], there is a great interest in using catalysts based on other more abundant and less expensive metals, such as Cu and Ce. Different formulations based on Cu and Ce oxides have been proposed [32–35], all of them presenting an excellent catalytic performance. But, to the best of our knowledge only one study has been published on the use of Cu–zeolite as catalyst for the COProx reaction [36].

The foregoing discussion explains our interest in developing microreactors for the CO oxidation, based on highly dispersed active phases of Cu and Ce on zeolite-coated brass microstructured substrates. The study focuses in first obtaining the dispersed active phase in the powder zeolite and then optimize the synthesis of zeolite coatings on brass microgrids in the search for continuous and stable films. Afterwards, Cu and Ce dispersed phases are introduced into the films and the obtained microreactors are evaluated in the total and preferential oxidation of CO.

2. Experimental

2.1. Support material and synthesis of zeolite coatings

We used strips of brass microgrids (Cu/Zn: 65/35) composed of wires of 100 μm in diameter with spaces of 140 μm between them (see Fig. 1). The substrates were previously washed first with water and then with acetone in an ultrasonic bath. The mordenite growth was performed by secondary synthesis using a gel containing colloidal silica (Ludox AS-40), Na_2Al_2O (Riedel-de-Häen), NaOH (Cicarelli pro-analysis) and distilled water, varying the dilution from H_2O:SiO_2 = 70:1.15 to 110:1.15. The reactants were aged by stirring for 2 h at r.t. and 100–200 nm sized crystals, extracted from a commercial zeolite powder (Na-Mordenite Zeolyst; Si/Al = 6.5), were used for the seeding. The seeds were obtained from the supernatant generated after centrifuging an aqueous suspension of the as received commercial powders, at 3500 rpm for 30 min. This zeolite was also used for the preparation of powder catalysts. Prior to the seeding, the microstructures were treated with a PDDA, poly(diallyldimethylammoniumchloride), aqueous solution (0.4 wt%). After that, the microgrids were submerged into a suspension of nanometric seeds (2 g L^{-1}) during 10 min. Then, the seeded supports were subsequently dried in N_2 flow (room temperature), and in a stove at 100 °C overnight. After seeding, the supports were placed vertically inside teflon-lined autoclaves and hydrothermally treated at 180 °C for 12–24 h. The internal autoclave was 60 cm^3 in volume and 40 mL of gel were used in all syntheses. After synthesis, the vessels were cooled and the samples were withdrawn from the autoclave, washed in water, treated in an ultrasonic bath for 10 min to remove residues from the solution and finally dried at 120 °C for 12 h. Table 1 summarizes the syntheses conditions.

2.2. Zeolite activation: Cu and Ce incorporation

The Cu incorporation in the powder zeolite as well as in zeolite-coated microreactors was carried out by ionic exchange with a 0.05 M $Cu(NO_3)_2$ solution of $(NO_3)_2Cu{\cdot}6H_2O$ (Aldrich®) for 24 h at pH = 5 and room temperature. Then, the samples were washed with distilled water and dried at 120 °C for 12 h. The subsequent addition of Ce was performed by impregnation with a colloidal CeO_2 suspension (Nyacol®, 10–20 nm). For the powder catalyst, Ce was added by incipient wetness impregnation whereas for microreactors, by washcoating with a slurry of 2% (w/w), blown with N_2 and drying at 120 °C. Subsequently, some samples were subjected to a reduction-oxidation (redox) treatment, similarly to a previously reported procedure [37]. The aim of this treatment was to generate clusters of copper oxide dispersed in the zeolite matrix. The reduction was carried out in a stream of H_2 in He (50%, v/v; 50 mL min^{-1}) at 350 °C during 2 h. Next, the oxidation was performed with O_2 in He (50%, v/v; 50 mL min^{-1}) for 1 h at the same temperature. Some samples without redox treatment were calcined at 350 °C for 2 h in air. The parent Na-Mordenite (Zeolyst) has a surface area of 409 m^2 g^{-1}, and after loading the active ingredients this value remained almost constant, due to the low amount of Cu and Ce incorporated by ionic exchange and impregnation, respectively. Table 2 presents a summary of the evaluated catalysts and microreactors.

2.3. Characterizations

2.3.1. Scanning electron microscopy (SEM)

The quality, orientation and microstructure of the zeolite films were examined by SEM with a Jeol JSM-35C equipment, operated

Table 1
Zeolite weight gain on microgrids treated under different synthesis conditions.

Sample	Support shape/size (mm)	Synthesis time (h)	Gel dilution (H_2O:SiO_2)	mg zeolite/cm^2 GSA
MZ1	Planar/20 × 20	12	70:1.15	1.02
MZ2	Planar/20 × 20	12	110:1.15	0.24
MZ3	Planar/20 × 20	24	110:1.15	0.98
MZ4	U/20 × 40	24	70:1.15	2.00
MZ5	Spiral/20 × 80	12	70:1.15	0.90
MZ6	Spiral/20 × 80	12 + 12	70:1.15	1.65
MZ7	Spiral/20 × 80	24	70:1.15	1.82

Table 2
Summary of the catalysts and methods of preparation.

Catalyst	Method of active phase incorporation
P(4-0)IE	Ionic exchange (IE)
P(4-0)IE-RO	Ionic exchange (IE) + redox (RO)
P(4-8)IE-IM-RO	Ionic exchange (IE) + impregnation (IM) + redox (RO)
P(4-4)IE-IM-RO	Ionic exchange (IE) + impregnation (IM) + redox (RO)
MZ	–
MZ(8-0)IE	Ionic exchange (IE)
MZ(10-0)IE	Ionic exchange (IE)
MZ(10-24)IE-IM	Ionic exchange (IE) + impregnation (IM)
MZ(10-2)IE-IM	Ionic exchange (IE) + impregnation (IM)
MZ(10-0.5)IE-IM	Ionic exchange (IE) + impregnation (IM)
MZ(10-4)IE-IM-RO	Ionic exchange (IE) + impregnation (IM) + redox (RO)
MZ(10-5)IE-IM-RO	ionic exchange (IE) + impregnation (IM) + redox (RO)

P: powder catalysts.
MZ: microreactor coated with zeolite film.
The estimated amount of Cu and Ce, respectively, is indicated between brackets.

at 20 kV. The samples were glued to the sample holder with Ag painting and then coated with a thin layer of Au in order to improve the images.

2.3.2. Electron probe micro analysis (EPMA) and elemental mapping

In order to study the distribution of the chemical elements present in the coating, a dispersive EDAX equipment coupled to the SEM Jeol JSM-35C was employed. The analyses were performed on broad areas in transversal sections of the coatings to get the global elemental composition and also in smaller selected areas at different locations. In this way, the compositional profiles in the coating thicknesses were obtained. The semiquantitative proportions of the elements were obtained by means of the SEMIQ method. Samples were put into a holder and covered with a thin film of graphite. For the elemental mapping a Zeiss FEG-SEM instrument, model SUPRA 40, equipped with an energy dispersive analytical system (Oxford Instruments) was employed.

2.3.3. X-ray diffraction (XRD)

A Shimadzu XD-D1 instrument operated with Cu Kα radiation at 40 kV and 30 mA was employed, with a scanning rate of 2° min^{-1} between $2\theta = 5°$ and 55° which is the range where the most important signals of the zeolite and Cu or Ce oxides can be found.

2.3.4. Temperature-programmed reduction with H_2 (H_2-TPR)

The H_2-TPR analyses were performed in an Okhura TP-2002S instrument equipped with a TCD detector and a molecular sieve 5 Å trap. The sample was first pretreated in situ with N_2 for 60 min at 300 °C before the experiments. After that, the sample was cooled at r.t. in N_2 flow and the TPR was run immediately in a 5% H_2–Ar stream (15 mL min^{-1}), heating at 10 °C min^{-1} up to the maximum treatment temperature.

2.3.5. Laser Raman spectroscopy (LRS)

LRS was performed on microreactors using a LabRam spectrometer (Horiba–Jobin–Yvon) coupled to an Olympus confocal microscope equipped with a CCD detector cooled to about 200 K. The excitation wavelength was 532 nm (Spectra Physics argon-ion laser). The laser power was set at 30 mW.

2.3.6. X-ray photoelectronic spectroscopy (XPS)

X-ray photoelectronic spectroscopy (XPS) analyses on microreactors surface were carried out in a SPECS system with a hemispherical PHOIBOS 150 analyzer operating in the fixed analyzer transmission (FAT) (Mg Kα X-ray source, 200 W and 12 kV; C 1s peak at 284.8 eV as internal reference). Spectra were acquired in the Cu 2p, Ce 3d, C 1s, Si 2p, and Al 2p regions The data processing and peaks deconvolution were performed using the Casa XPS software. Peaks were fitted by a Gaussian–Lorentzian component wave-form after an inelastic (Shirley-type) background had been subtracted.

2.3.7. Coating adherence

The adherence of zeolite coatings was evaluated subjecting the microreactors to an agressive mechanical stability test consisting in an ultrasound treatment we had previously performed on other types of zeolite coatings [38]. The microreactors were immersed in water inside a glass vessel and then in an ultrasonic bath (Cole Parmer, 47 kHz and 130 W) at 25 °C for 1 h. After that, the samples were dried at 120 °C during 8 h and the weight of the samples were measured both before and after the treatment.

2.4. Catalytic evaluations

The powder catalysts and microreactors were evaluated in a continuous flow system equipped with flow mass controllers (MKS). The composition of the reaction flow for COTox was 1% CO, 2–20% O_2 in He balance. For the COProx reaction the composition was 1% CO, 2% O_2, 40% H_2 in He balance. CO concentration was fixed in this value because it is the usual one for testing catalysts for both COTox and COProx reactions. Oxygen concentration was varied from 2% to 20% in COTox in order to study its effect on CO conversion. The reactions, both for powders and microgrids reactors, were carried out in a glass tubular reactor (6 mm inner diameter) heated by a furnace with temperature controller at temperatures between 75 °C and 350 °C with flow/mass ratio (F/W) of 330 mL(STP) min^{-1} g^{-1} (Typically 60 mg of catalyst, both for powders and microreactors, and a total flow of 20 mL(STP) min^{-1} were used). The microreactors were assembled rolling a zeolite-coated microgrid around a small brass cylinder, which prevented a bypass flow (Fig. 2b). In this way, the reactants flowed perpendicular to the microgrid section (which is a front section) shown in Fig. 2a. The catalytic channels (100–140 μm size) were defined by the separation between the wires of the grid.

This configuration is similar to that used with mesoporous Co_3O_4 nanowire arrays supported on a stainless steel grid [39]. Prior to the evaluation, the samples were dried in situ under He flow at 120 °C and after that the reaction mixture was fed. The analyses of the gases were performed with a Shimadzu GC-2014 chromatograph equipped with a TCD detector and a column of zeolite 5A. CO conversions were calculated as: $X_{CO} = [CO]^o - [CO]/[CO]^o$; where X is conversion, $[CO]^o$ and [CO] are inlet and outlet gas concentrations in ppm, respectively. For COProx reaction selectivity was calculated as $S_{CO} = 1/2([CO_2]/[O_2]^o - [O_2])$.

3. Results and discussion

3.1. Optimization of the powder catalysts

XRD patterns of the powder catalysts obtained by the ion exchange-impregnation-redox procedure are shown in Fig. 3. It can be observed that the crystallinity of the zeolite was not affected by any of the procedures, keeping the characteristic signals of mordenite unchanged, while in the sample treated by redox a weak reflection of CuO at $2\theta = 38.5$ was detected (JCPDS 44-706). The other main signal of this oxide ($2\theta = 35.3°$) overlaps the signals of the zeolite. In the sample with a further impregnation with CeO_2, as expected, weak reflections were observed at $2\theta = 28.8°$ and 47.5° corresponding to the crystalline phase of the said oxide (ICDD 34-0394). In this sample, the CuO signals were very weak. The H_2-TPR profiles of these samples are presented in Fig. 4. The Cu-exchanged sample (P(4-0) IE) shows three main reduction peaks. According to the literature, the reduction of Cu species in zeolites occurs in two stages: (1) reduction of exchanged Cu(II) to

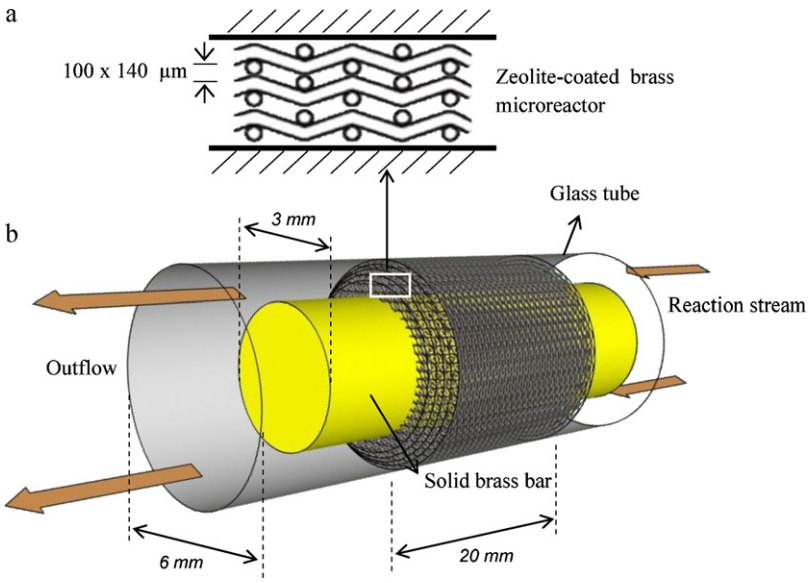

Fig. 2. Scheme of the assembled microreactor: (a) frontal section of microgrid and (b) constructive details and dimensions.

Cu(I) and reduction of dispersed CuO to Cu(0), and (2) reduction of exchanged Cu(I) to Cu(0) [40]. The correspondence of our pattern with these processes and with other H_2-TPR profiles of Cu-mordenite with similar copper content [41,42] implies that signals at 204 °C, 257 °C and 390 °C are coming from exchanged Cu(II), dispersed CuO from not exchanged ions and exchanged Cu(I), respectively. When this sample was further treated by redox, the TPR profile was modified (Fig. 4) a new signal appearing around 165 °C which is attributed to highly dispersed CuO. The generation of such dispersed species, which presented lower reduction temperatures than those of Cu(II), can also be produced by the ion-exchange processes alone, as has been shown by De Lucas et al. [43]. The rest of the profile remained basically similar, with a slight modification of the signal around 200 °C, which may be due to a redistribution of CuO particle sizes caused by the redox treatment. On the other hand, when CeO_2 was added (P(4-8) IE-IM-RO), an increased consumption in the 250–350 °C range and a shift towards lower values of the Cu(I) signal were observed. This is due to a synergy between CeO_2 and Cu species [44] so that CeO_2 and Cu(I) species are easily reduced, the former appearing overlapped to Cu(II) signals in the 250–350 °C region.

Fig. 5 shows the catalytic CO conversion curves of these catalysts. The Cu-exchanged solid presented a similar behavior to that of redox-treated sample, indicating a small difference in activity between the different Cu species. However, the sample with highly dispersed CuO seems to have a slightly higher activity. Instead, when CeO_2 was added a marked increase in activity was observed which followed the trend in samples with a higher CeO_2 content. A similar behavior was observed in other CuO/CeO_2 catalysts, which also presented optimum proportions of Cu and Ce [45]. It is known that the improved activity in this catalytic phase is the result of a synergistic effect developed at the interface of the particles of both oxides [46]. Then, from the catalytic performance and characterization results it can be inferred that in the Cu–Ce redox treated sample, there is a high interaction between the dispersed CuO and CeO_2 particles. Probably this synergy occurs at the outside of the

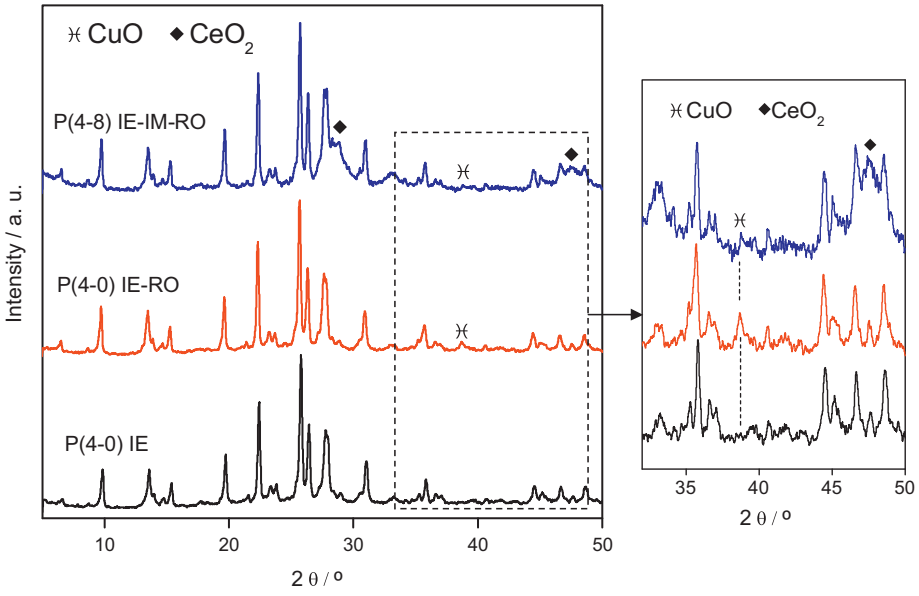

Fig. 3. XRD patterns of Cu–Ce/mordenite powder catalysts.

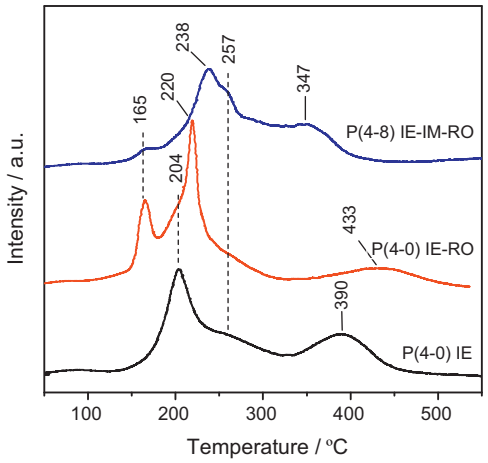

Fig. 4. H_2-TPR profiles of Cu–Ce/mordenite powder catalysts.

zeolite crystals, since CeO_2 nanoparticles (10–20 nm) cannot enter into the pores of this zeolite. The Ce–Cu synergic effect was pronounced for the samples subjected to the redox treatment, fact that is originated in the segregation of CuO which can interact better with CeO_2 than exchanged Cu. Thus, we consider that both redox treatment and Ce impregnation are equally important factors in improving the catalytic activity.

The above results show the feasibility of obtaining active phases of CuO–CeO_2 highly dispersed in a zeolite matrix by the ion exchange-impregnation-redox treatment. The objective of the optimization of this procedure was to subsequently apply it to a film configuration in microreactors. Next, we discuss the synthesis and optimization of mordenite coatings onto the microreactor supports.

3.2. Synthesis of mordenite coatings on brass microgrids

In order to determine the conditions of preparation of films with optimal qualities, zeolite synthesis experiments were performed as shown in Table 1. Before the hydrothermal treatment the supports were seeded as discussed before. Synthesis time, gel dilution and size/geometry of the substrates were modified. In relation to the latter, small pieces of planar-shaped, U-shaped and spiral-shaped samples with sizes of 20 mm × 20 mm (MZ1, MZ2, MZ3), 20 mm × 40 mm (MZ4) and 20 mm × 80 mm (MZ5, MZ6), respectively, were subjected to synthesis (as shown in Fig. 1). After conducting a hydrothermal treatment of the seeded support for

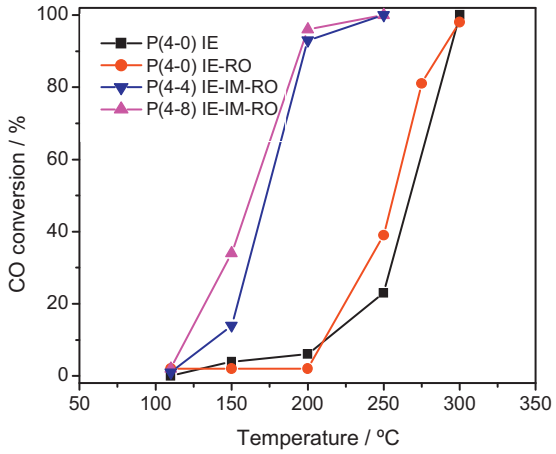

Fig. 5. Catalytic CO oxidation curves of Cu–Ce/mordenite powder catalysts.

Table 3
EPMA profile of the mordenite coating in a microreactor.

Coating sector	Si/Al[a]	Cu/Al[a]	Zn/Al[a]
1-Top of the film	8.77	0.62	0.15
2-External middle of the film	9.00	0.67	0.11
3-Internal middle of the film	8.89	0.89	0.22
4-Interface substrate-coating	6.77	2.44	0.88
5-Substrate (Cu/Zn = 1.88)	–	–	–

[a] Atomic ratios.

12 h (MZ1) there was a growth of pure mordenite, in view that all the main XRD indexed reflections for this phase (not shown) were determined [47]. Table 1 shows the zeolite weight gain per geometric surface area (GSA) of the support. For the MZ1 sample, the gain was high, probably due to the large surface area available for the film growth (~250 cm^2 GSA/cm^2 of grid). SEM observations of this sample (Fig. 6a) indicated that growth occurred evenly over the entire surface of the wires. The film consisted of nano-crystals arranged vertically from the surface (c-orientation), with low intergrowth. However, when the synthesis gel employed was more diluted, the mass gain achieved was lower but when the synthesis time doubled, the weight gain increased four times (Table 1). Moreover, a denser coating was obtained in this latter case (Fig. 6b), with a higher intergrowth and with crystals oriented in a more horizontal position with respect to the substrate. When the hydrothermal treatment was conducted for 24 h under the same conditions as for MZ1 but with the U-shaped substrate, a higher zeolite mass gain was obtained (Table 1). This is in agreement with the higher intensity of the XRD reflections observed for this sample. Additionally, the crystallographic orientation in b was more accentuated as can be seen in the top view of the coating (Fig. 6c). We have previously observed that such crystal orientation is favorable because it leaves the channels of this zeolite parallel to the reaction stream [48]. As a matter of fact, the mordenite structure has main channels of 12 MR with a size of 7 Å × 6.5 Å, and smaller 8 MR side pockets of 2.6 Å × 5.7 Å. Thus, the free diffusion of molecules inside the main channels is favored by the indicated orientation. Equally important is the sensitivity of the crystallographic orientation produced with the single modification of the support geometry, which may be associated with changes in the local concentration of reagents in the vicinity of the support surface. In this sense, it has been proposed that the zeolite film orientation is influenced by its immediate growth environment [49]. When the synthesis was performed onto supports in spiral geometry, the coatings showed a microstructure similar to that obtained with the U-shaped support. In this case, the weight gain was also proportional to the synthesis time with a slight decrease for the MZ6 sample. From these synthesis experiments we selected the conditions used in MZ7 for the preparation of the zeolite-based microreactors. As can be seen the growths obtained were homogeneous and about 10 μm in thickness.

Elemental mappings performed in cross sections of the growths (Fig. 7) showed that in addition to the zeolite elements, Cu and Zn were present. This indicates that the substrate is partially dissolved during the synthesis, due to the strongly basic medium employed. Since Cu and Zn were accumulated at the substrate-coating interface, as shown in the mapping, it follows that the dissolution occurred mainly during the early stages of the synthesis. Moreover, the overall elemental composition of the zeolite coating (Si, Al, O, Na) was consistent with the theoretical composition for this zeolite [47]. In addition, localized elemental compositions were taken at different depths in the growths as indicated in Fig. 7 and presented in Table 3. The nominal alloy composition of the support was Cu/Zn = 1.88. The trends in the composition of the coatings showed a Si/Al ratio that decreased towards the interface, reaching a value of 6.77, and that Cu and Zn of the support migrated to the film, in line with the previous mapping.

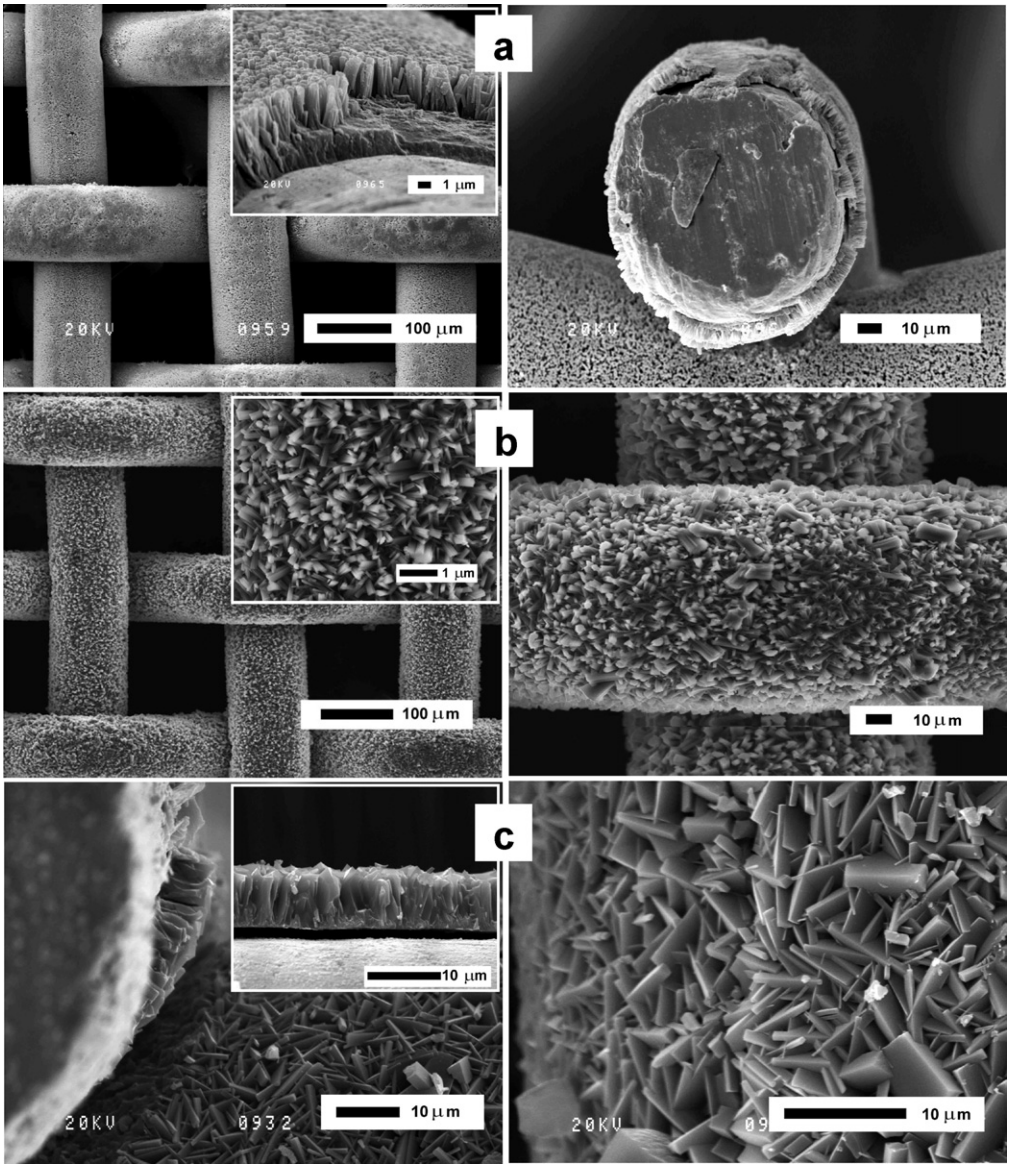

Fig. 6. SEM of zeolite films synthesized onto brass microgrids: (a) MZ1 sample; (b) MZ3 sample; (c) MZ4 sample.

The zeolite-coated microstructures subjected to a 60-min ultrasonic test showed no mass loss, which indicated a high adhesion of the coatings. Previously, we had also seen a good adhesion of this type of zeolite coating synthesized in microchannels of the same material [16]. This quality was also appreciated in the SEM images (Fig. 6), where it was noted that the coating remained firmly attached to the substrates despite the cuts and handling made for the observations. Summarizing, it can be said that it was possible to synthesize homogeneous and stable coatings of mordenite onto brass microgrids. After that, Cu and Ce species were incorporated

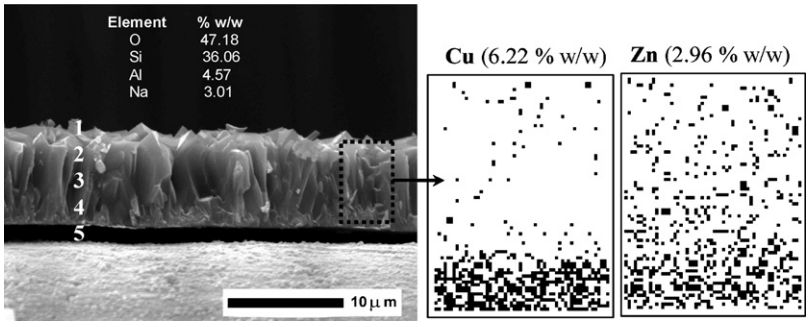

Fig. 7. SEM image and elemental mapping in a cross section of a mordenite-coated microreactor.

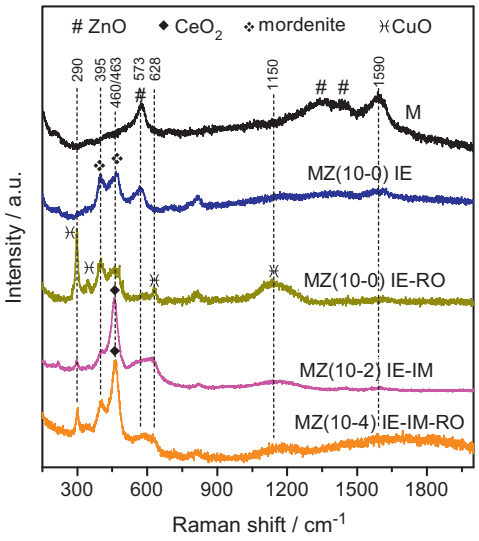

Fig. 8. LRS spectra on Cu–Ce/mordenite microreactors.

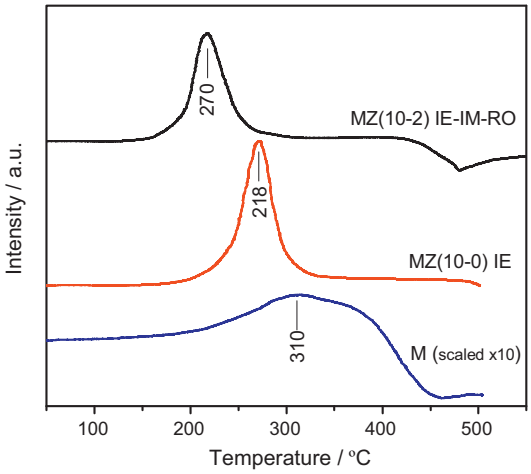

Fig. 9. H_2-TPR profile of Cu–Ce/mordenite microreactors.

through the ionic exchange-impregnation-redox procedure, as previously discussed for the powder catalysts. The characterizations of these catalytic films are presented next.

3.3. Microreactors based on Cu, Ce–mordenite coatings

3.3.1. Characterization of active species loaded to the coatings

Fig. 8 shows the LRS spectra performed on the zeolite-coated and uncoated microreactors. In the latter, three signals were observed at 573, 1350 and 1439 cm^{-1} that could be assigned to bulk ZnO [50,51] present at the support surface, while typical bands of graphitic carbon at 1339 and 1590 cm^{-1} were also present. In contrast, for the sample with the Cu-exchanged zeolite film new signals appeared in the range of 600–300 cm^{-1}. This is the range in which the most intense Raman bands of zeolites are usually observed due to the symmetrical T–O–T bending modes [52]. Particularly, the signals at 395 cm^{-1} and 460 cm^{-1} are characteristic of mordenite [53]. In addition to the above signals, in the Cu-exchanged coating with the redox treatment, new bands at 290, 340, and 628 cm^{-1} developed as well as a broad band at 1150 cm^{-1}. These bands are typical of CuO [54] and verifies the success of the redox process to disperse this phase on the microreactor coatings. Furthermore, when ceria was incorporated the most intense band of this oxide at 463 cm^{-1} [55] was also observed. By H_2-TPR (Fig. 9) it can be seen that the uncoated substrate showed a very weak and broad signal between 400 and 600 °C, which declined after 400 °C. The appearance of this profile is very similar to that reported for bulk ZnO [56], in line with the previous LRS results. Moreover, the first part of this signal may have a contribution of bulk CuO. When the substrate was coated with a Cu-exchanged mordenite film, CuO species showed a signal with a maximum around 260 °C. Different from what happened in the powder catalysts, it was not possible here to distinguish the contributions of the different species and they should be included under the same reduction peak. In the Cu, Ce–containing coating, even though the profile shape was similar it shifted towards lower temperatures. As discussed above, this effect shows an effective interaction between CeO_2 and Cu species which implies an effective dispersion of these phases on the zeolite coating. A close-up view of the coatings before and after the redox treatment (Fig. 10) showed that this procedure did not produce observable changes in the microstructure of the zeolite crystals. However, a thin layer, cracked in certain areas, covering zeolite crystals can be noticed in the sample before the treatment (Fig. 10a). This should correspond to an uniformly distributed CeO_2 film. Whereas, in the sample after the redox treatment (Fig. 10b) there appeared small aggregates about 20 nm that should be small CeO_2 particles generated during the redox treatment. It was previously observed by H_2-TPR that CeO_2 in the presence of Cu species is reduced at temperatures between 250 and 350 °C which is the range used during the first step of the redox treatment. Then, small aggregated clusters of Ce(III) can be formed which are transformed into CeO_2 after the next oxidation step.

The surface analyses by XPS showed for the zeolite-coated substrate (MZ) a weak Cu $2p_{3/2}$ signal (Fig. 11a) with contributions of Cu(I) and Cu(II) species [57], as indicated in Table 4. On the other hand, the Si/Al surface ratio of the zeolite was in the order of the one determined by EPMA, with a slight enrichment in Al. Additionally, Na 1s signal was observed giving a Na/Al ratio of 1.1, while in the other samples no Na signal was detected. On the other hand, for the Cu-exchanged zeolite coating with a redox treatment an aluminum surface segregation was observed (Table 4) which could be due to a partial zeolite dealuminización caused by the output of Cu species from exchange sites during the redox treatment. Simultaneously, an increase in the proportion of Cu(I) and Cu(II) due to the ion exchange and generation of CuO, respectively, was observed (Fig. 11a). Meanwhile, in the microreactors containing Ce and used in reaction, an increased proportion of Cu(I) species was noticed, while Ce 3d signals were also observed (Fig. 11b). It can be seen that there was a mixture of Ce(III) and Ce(IV) [58], with a surface enrichment in Ce(IV) (Table 4). This could be due to the generation of O vacancies in the CeO_2 structure during the CO oxidation. The Ce(III) present at the Cu–Ce interphase may be responsible for the increased proportion of Cu(I) given under the CO atmosphere.

3.3.2. Catalytic performance of microreactors

Fig. 12a shows that the microreactor without the catalytic coating (M) was active in the oxidation of CO with a total conversion at 300 °C. The activity in this sample is ascribed to the small proportion of CuO at substrate surface, which in addition has a high contact surface. In contrast, in the microreactor coated with the zeolite (MZ), the catalytic activity was increased due to the presence of a higher proportion of CuO species (ca. 4 wt%) dispersed in the zeolite film as a consequence of the partial support dissolution during synthesis. The zeolite by itself does not play a significant role in the CO oxidation reaction; the active components are the Cu incorporated by ionic exchange and the Ce loaded by impregnation of cerium oxide nanoparticles. The mordenite structure acts as the support of the said active components, and constitutes a homogeneous and stable film with high surface area. By increasing the Cu

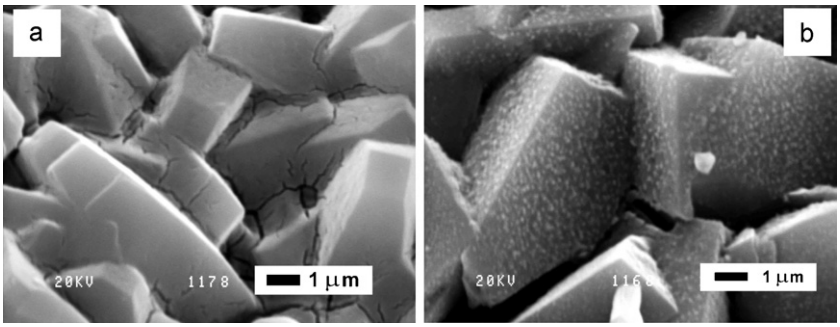

Fig. 10. SEM images of Cu–Ce/mordenite coating (MZ(10-5)IE-IM): (a) before and (b) after redox treatment.

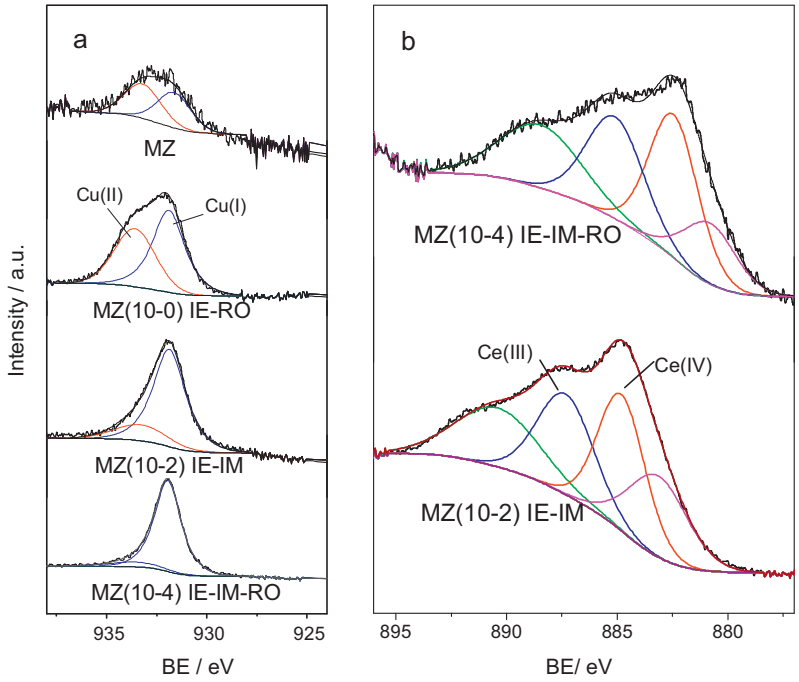

Fig. 11. XPS spectra on microreactor coatings in the Cu $2p_{3/2}$ and Ce 3d regions.

content in the zeolite film by ion exchange, the activity followed the same trend. Meanwhile, in the Cu–Ce/zeolite microreactors (Fig. 12b) an optimum CeO_2 loading was observed, in which the activity was maximum. Once the amount of ceria necessary to interact with the dispersed CuO was reached, the excess did not give new active sites at the CuO–CeO_2 interface. Subsequently, in a Cu–Ce/zeolite microreactor containing the optimal Cu/Ce ratio a redox treatment was carried out (MZ(10-4) IE-IM-RO). The catalytic performance of this sample was clearly higher, reaching complete conversion at 175 °C with a T^{50} of 117 °C. Compared with the powder catalysts, a significant improvement can be seen in the activity of the microstructured catalytic configuration. The positive effect of the Ce impregnation when performed in the Cu-exchanged mordenite/microgrids is marked because during the synthesis, process Cu from the brass grids migrated inside the mordenite structure generating CuO crystals that interacted with CeO_2. When the redox treatment was applied after the Cu exchange, more CuO was generated, which further improved the beneficial effect of Ce.

Another microreactor prepared identically to that discussed above (MZ (10-5) IE-IM-RO) presented a similar catalytic performance (Fig. 12b), which implies that the microreactor preparation methodology has a good reproducibility. Moreover, this microreactor showed good chemical stability, and no deactivation after 20 h at 110 °C under reaction conditions (ca. 38% of CO conversion). Table 5 presents a summary of the catalytic performance of all evaluated samples, expressing the conversion at 150 °C (X^{150}) divided

Table 4
XPS results on the catalytic coatings.

Sample	Cu(I) $2p_{3/2}$(fwhm)[a]	Cu(II) $2p_{3/2}$ (fwhm)	Ce(III) $3d_{3/2}$ (fwhm)	Ce(IV) $3d_{5/2}$ (fwhm)	Ce(III)/Ce(IV)	Si/Al
MZ	931.6 (2.0)	933.2 (2.1)	–	–	–	5.29
MZ(10-0)IE-RO	931.9 (1.9)	933.6 (2.4)	–	–	–	3.12
MZ(10-2)IE-IM	931.9 (1.9)	933.3 (3.0)	885.2 (3.0)	882.7 (2.5)	0.53	nd[b]
MZ(10-4)IE-IM-RO	931.9 (1.5)	933.5 (3.0)	885.1 (3.0)	882.4 (2.6)	0.50	nd[b]

C 1s peak at 284.8 eV was taken as internal reference.
[a] Binding Energy (eV).
[b] Not determined because of the strong superposition between Ce 4d-Si 2p and Cu 3p-Al 1s signals, difficult the deconvolution of the peaks.

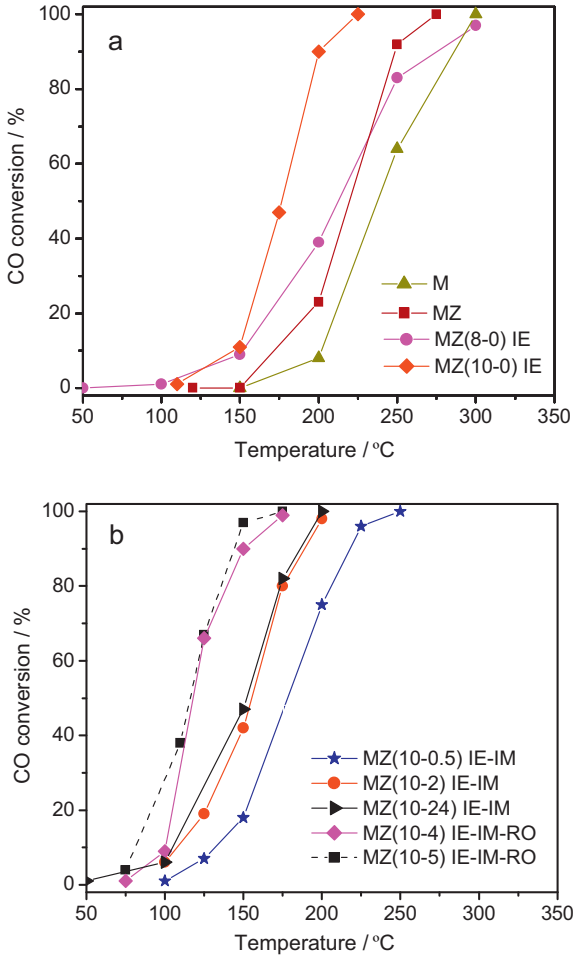

Fig. 12. Catalytic CO oxidation (COTox) curves of microreactors: (a) Cu/mordenite microreactors and (b) Cu–Ce/mordenite microreactors.

by the Cu loading and the temperature at which 50% conversion was reached (T^{50}). It is true that the activity of catalysts is also affected by the Ce loading, but since it has been reported that Cu is the active phase and CeO_2 acts as a surface oxygen donor [45], we decided to relate conversions to the Cu loadings in order to make comparisons between catalysts.

The catalytic improvement achieved with the microreactors in comparison to the CuO–CeO_2/mordenite powder catalysts is due to several reasons: the high geometric surface area which provides a large contact surface between the reaction stream and the catalytic coating; the configuration and size of microchannels

Table 5
Summary of catalytic performance of all catalysts.

Catalyst	X^{150}/Cu (mg)	T^{50} (°C)
P(4-0)IE	1.6	267
P(4-0)IE-RO	1.7	256
P(4-8)IE-IM-RO	14.2	162
P(4-4)IE-IM-RO	9.8	172
MZ	2.1	220
MZ(8-0)IE	3.5	212
MZ(10-0)IE	4.3	176
MZ(10-24)IE-IM	9.3	152
MZ(10-2)IE-IM	10.7	154
MZ(10-0.5)IE-IM	4.1	177
MZ(10-4)IE-IM-RO	27.7	117
MZ(10-5)IE-IM-RO[a]	26.8	144

T^{50}: temperature of 50% conversion.
[a] Sample evaluated in COProx reaction.

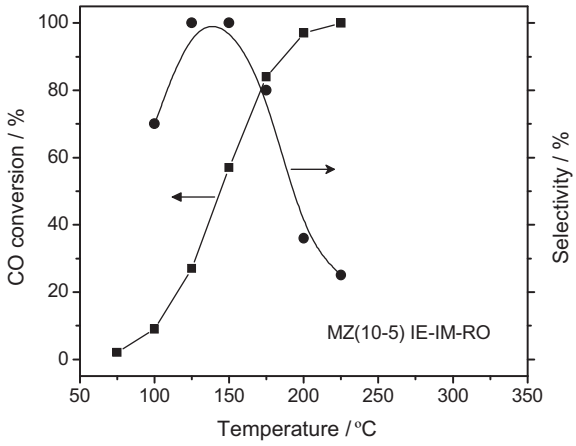

Fig. 13. Catalytic CO preferential oxidation (COProx) in a Cu–Ce/mordenite microreactor.

between 100 and 140 μm which ensures a proper flow regime to achieve high mass transfer rates; the nature of the substrate which is capable of generating an extra amount of CuO both in its surface and in the zeolite film during the synthesis process; the better dissipation of reaction heat from the film due to the excellent thermal properties of the support can reduce hot spots and active phase sinterization. In view of the good performance of these microreactors in the COTox reaction they were also evaluated in the COProx reaction. Fig. 13 shows the activity curve for the MZ (10-5) IE-IM-RO microreactor, in which a complete conversion at 220 °C was achieved, whereas the selectivity showed a maximum near 150 °C. This represents a good behavior for this catalytic phase. The displacement of the conversion curves to higher temperatures compared with those of COTox (Table 5), may be due to a lower O_2 availability by the competitive process of H_2 combustion. The temperatures in which high CO conversions and selectivity were reached are compatible with that of streams from water–gas shift processes, whereupon the microreactor may be adapted to further purify the H_2 stream. Moreover, given the excellent heat transfer properties and maleability of these microreactors it is possible to design a configuration in which they are coupled to that endothermic reaction improving the overall thermal balance.

4. Conclusions

Homogeneous mordenite films were synthesized on brass microgrids and later incorporated with dispersed phases of CuO and CeO_2, which were successfully employed as microreactors for the CO oxidation. The 10 μm thickness films were strongly adherent and homogeneously synthesized on the entire support. These films were loaded with CuO and CeO_2 nanoparticles in close interaction through a sequential procedure comprising Cu ionic exchange, impregnation with colloidal CeO_2, followed by a redox treatment at high temperature. The Cu, Ce/zeolite-based microreactors achieved a higher catalytic performance compared with that of the same catalysts in powder shape, probably due to the great dispersion of active centers acting in the micrometer-sized channels which yields a large catalytic surface area in a small volume. The microreactor combines a stable catalytic coating activated with non-noble metals synthesized onto a high thermal conductivity and low costly support in a simple configuration.

Acknowledgements

The authors wish to acknowledge the financial support received from Universidad Nacional del Litoral, CONICET, and ANPCyT. Thanks are given to Elsa Grimaldi for the English language editing.

References

[1] G. Kolb, V. Hessel, Chemical Engineering Journal 98 (2004) 1–38.
[2] L. Kiwi-Minsker, A. Renken, Catalysis Today 110 (2005) 2–14.
[3] P.L. Mills, D.J. Quiram, J.F. Ryley, Chemical Engineering Science 62 (2007) 6992–7010.
[4] G. Groppi, G. Airoldi, C. Cristiani, E. Tronconi, Catalysis Today 60 (2000) 57–62.
[5] M.J.M. Mies, E.V. Rebrov, M.H.J.M. de Croon, J.C. Schouten, Chemical Engineering Journal 101 (2004) 225–235.
[6] I.Z. Ismagilov, E.M. Michurin, O.B. Sukhova, L.T. Tsykoza, E.V. Matus, M.A. Kerzhentsev, Z.R. Ismagilov, A.N. Zagoruiko, E.V. Revrov, M.H. de Croon, J.C. Schouten, Chemical Engineering Journal 135S (2008) S57–S65.
[7] P. Pfeifer, K. Schubert, M.A. Liauw, G. Emig, Applied Catalysis A-General 270 (2004) 165–175.
[8] C. Horny, L. Kiwi-Minsker, A. Renken, Chemical Engineering Journal 101 (2004) 3–9.
[9] W.D. Callister Jr., Fundamentals of Materials Science and Engineering, second ed., John Wiley & Sons, New York, 2005.
[10] O. Sanz, S.A. Cruz, J.C. Millán, M. Montes, J.A. Odriozola, Studies in Surface Science and Catalysis 175 (2010) 661–664.
[11] E.V. Rebrov, G.B.F. Seijger, H.P.A. Calis, M.H.J.M. de Croon, C.M. van den Bleek, J.C. Schouten, Applied Catalysis A 206 (2001) 125–143.
[12] O. de la Iglesia, V. Sebastián, R. Mallada, G. Nikolaidis, J. Coronas, G. Kolb, R. Zapf, V. Hessel, J. Santamaría, Catalysis Today 125 (1–2) (2007) 2–10.
[13] A. Eleta, P. Navarro, L. Costa, M. Montes, Microporous and Mesoporous Materials 123 (2009) 113–122.
[14] Y.S.S. Wan, J.L.H. Chau, A. Gavriilidis, K.L. Yeung, Microporous and Mesoporous Materials 42 (2001) 157–175.
[15] G. Yang, X. Zhang, S. Liu, K.L. Yeung, J. Wang, Journal of Physics and Chemistry of Solids 68 (2007) 26–31.
[16] J.M. Zamaro, E.E. Miró, Catalysis Communications 10 (2009) 1574–1576.
[17] V. Sebastian, S. Irusta, R. Mallada, J. Santamaría, Catalysis Today 147S (2009) S10–S16.
[18] M.J.M. Mies, E.V. Rebrov, J.C. Jansen, M.H.J.M. de Croon, J.C. Schouten, Journal of Catalysis 247 (2007) 328–338.
[19] N. Navascués, M. Escuin, Y. Rodas, S. Irusta, R. Mallada, J. Santamaría, Industrial & Engineering Chemistry Research 49 (2010) 6941–6947.
[20] Y.S.S. Wan, J.L.H. Chau, K.L. Yeung, A. Gavriilidis, Journal of Catalysis 223 (2004) 241–249.
[21] X. Zhang, E.S.M. Lai, R.M. Aranda, K.L. Yeung, Applied Catalysis A 261 (2004) 109–118.
[22] I. Yuranov, A. Renken, L. Kiwi-Minsker, Applied Catalysis A-General 281 (2005) 55–60.
[23] S.P. Davis, E.V.R. Borgstedt, S.L. Suib, Chemistry of Materials 2 (1990) 712–719.
[24] S. Mintova, V. Valtchev, L. Konstantinov, Zeolites 17 (1996) 462–465.
[25] V. Valtchev, S. Mintova, Zeolites 15 (1995) 171–175.
[26] S. Mintova, V. Valtchev, L. Konstantinov, Zeolites 15 (1995) 679–683.
[27] L. Bonaccorsi, A. Freni, E. Proverbio, G. Restuccia, F. Russo, Microporous and Mesoporous Materials 91 (2006) 7–14.
[28] E. Green, S. Short, IEH Assessment on Indoor Air Quality in the Home (2): Carbon Monoxide, Leicester, 1998.
[29] H. Igarashi, T. Fujino, M. Watanabe, Journal of Electroanalytical Chemistry 391 (1995) 119–123.
[30] J.L. Ayastuy, M.P. González-Marcos, J.R. González-Velasco, M.A. Gutiérrez-Ortiz, Applied Catalysis B 70 (2007) 532–541.
[31] C. Galletti, S. Fiorot, S. Specchia, G. Saracco, V. Specchia, Chemical Engineering Journal 134 (2007) 45–50.
[32] P. Doggalia, S. Waghmarea, S. Rayalua, Y. Teraokab, N. Labhsetwar, Journal of Molecular Catalysis A-Chemical 347 (2011) 52–59.
[33] K.N. Rao, P. Bharali, G. Thrimurthulu, B.M. Reddy, Catalysis Communications 11 (2010) 863–866.
[34] H. Mai, D. Zhang, L. Shi, T. Yan, H. Li, Applied Surface Science 257 (2011) 7551–7559.
[35] A. Razegui, A. Khodadadi, H. Ziaei-Azad, Y. Mortazavi, Chemical Engineering Journal 164 (2010) 214–220.
[36] T.R.O. Souza, A.J.S. Mascarenhas, H.M.C. Andrade, Reaction Kinetics and Catalysis Letters 87 (2006) 3–9.
[37] C.-Y. Lee, T.-H. Jung, B.-H. Ha, Applied Catalysis B 9 (1996) 77–91.
[38] J.M. Zamaro, M.A. Ulla, E.E. Miró, Chemical Engineering Journal 106 (2005) 25–33.
[39] G. Marbán, I. López, T. Valdés-Solís, A.B. Fuertes, International Journal of Hydrogen Energy 33 (2008) 6687–6695.
[40] G. Delahay, B. Coq, L. Broussous, Applied Catalysis B 12 (1997) 49–59.
[41] C. Torre-Abreu, C. Henriques, F.R. Ribeiro, G. Delahay, M.F. Ribeiro, Catalysis Today 54 (1999) 407–418.
[42] B. Coq, D. Tachon, F. Figukas, G. Mabilon, M. Prigent, Applied Catalysis B 6 (1995) 271–289.
[43] A. De Lucas, J.L. Valverde, F. Dorado, A. Romero, I. Asencio, Journal of Molecular Catalysis A-Chemical 225 (2005) 47–58.
[44] T. Caputo, L. Lisi, R. Pirone, G. Russo, Applied Catalysis A 348 (2008) 42–53.
[45] M. Jobbágy, F. Mariño, B. Schonbrod, G. Baronetti, M. Laborde, Chemistry of Materials 18 (2006) 1945–1950.
[46] A. Martínez-Arias, D. Gamarra, M. Fernández-García, X.Q. Wang, J.C. Hanson, J.A. Rodriguez, Journal of Catalysis 240 (2006) 1–7.
[47] D.W. Breck, Zeolite Molecular Sieves, John Wiley & Sons, New York, 1974.
[48] J.M. Zamaro, M.A. Ulla, E.E. Miró, Applied Catalysis A 308 (2006) 161–171.
[49] S.M. Lai, L.T.Y. Au, K.L. Yeung, Microporous and Mesoporous Materials 54 (2002) 63–77.
[50] L. Yohai, W.H. Schreiner, M. Vázquez, M.B. Valcarce, Applied Surface Science 257 (2011) 10089–10095.
[51] S.S. Kanmani, K. Ramachandran, Renewable Energy 43 (2012) 149–156.
[52] Y. Huang, R.M. Paroli, A.H. Delgado, T.A. Richardson, Spectrochimica Acta-Part A 54 (1998) 1347–1354.
[53] P. Knops-Gerrits, D.E. De Vos, E.J.P. Feijen, P.A. Jacobs, Microporous and Mesoporous Materials 8 (1997) 3–17.
[54] M.-F. Luo, P. Fang, M. He, Y.-L. Xie, Journal of Molecular Catalysis A-Chemical 239 (2005) 243–248.
[55] S. Wang, W. Wang, J. Zuob, Y. Qian, Materials Chemistry and Physics 68 (2001) 246–248.
[56] M. Liang, W. Kang, K. Xie, Journal of Natural Gas Chemistry 18 (2009) 110–113.
[57] M.C. Biesinger, L.W.M. Lau, A.R. Gerson, R.St.C. Smart, Applied Surface Science 257 (2010) 887–898.
[58] Y.A. Teterin, A.Yu. Teterin, A.M. Lebedev, I.O. Utkin, Journal of Electron Spectroscopy and Related Phenomena 88–91 (1998) 275–279.